ARL-TR-7799 ● SEP 2016

US Army Research Laboratory

A Discrete Scatterer Technique for Evaluating Electromagnetic Scattering from Trees

by DaHan Liao

NOTICES

Disclaimers

The findings in this report are not to be construed as an official Department of the Army position unless so designated by other authorized documents.

Citation of manufacturer's or trade names does not constitute an official endorsement or approval of the use thereof.

Destroy this report when it is no longer needed. Do not return it to the originator.

ARL-TR-7799 ● SEP 2016

US Army Research Laboratory

A Discrete Scatterer Technique for Evaluating Electromagnetic Scattering from Trees

by DaHan Liao
Sensors and Electron Devices Directorate, ARL

REPORT DOCUMENTATION PAGE

Form Approved
OMB No. 0704-0188

1. REPORT DATE *(DD-MM-YYYY)*	2. REPORT TYPE	3. DATES COVERED (From - To)
September 2016	Technical Report	2015–2016

4. TITLE AND SUBTITLE
A Discrete Scatterer Technique for Evaluating Electromagnetic Scattering from Trees

5a. CONTRACT NUMBER

5b. GRANT NUMBER

5c. PROGRAM ELEMENT NUMBER

6. AUTHOR(S)
DaHan Liao

5d. PROJECT NUMBER

5e. TASK NUMBER

5f. WORK UNIT NUMBER

7. PERFORMING ORGANIZATION NAME(S) AND ADDRESS(ES)
US Army Research Laboratory
ATTN: RDRL-SER-U
2800 Power Mill Road
Adelphi, MD 20783-1138

8. PERFORMING ORGANIZATION REPORT NUMBER
ARL-TR-7799

9. SPONSORING/MONITORING AGENCY NAME(S) AND ADDRESS(ES)

10. SPONSOR/MONITOR'S ACRONYM(S)

11. SPONSOR/MONITOR'S REPORT NUMBER(S)

12. DISTRIBUTION/AVAILABILITY STATEMENT
Approved for public release; distribution is unlimited.

13. SUPPLEMENTARY NOTES

14. ABSTRACT
An analytical solver is developed for characterizing the coherent scattering responses of trees. Realistic 3-D tree structures are first constructed using an open-source random tree generation engine. The trees are then parsed into discrete, canonical scatterers, such as cylinders and disks, and a multi-ray approach is applied for the calculation of the aggregate response of the scene, with the transmissivity of each ray determined from a cell-based representation of the computational domain. As each scatterer in the outlined framework is assigned a deterministic position, the spatial distribution of the trees and their canopy structures is fully preserved. A cell-by-cell strategy is also proposed for speeding up the calculations of the responses from small components such stems and leaves, which are expected to far outnumber those scatterers composing the main trunks. The accuracy of the analytical solver is assessed by comparing simulation results for a forest stand with solutions from a large-scale, full-wave solver. The primary aim of this study is to develop an accurate and computationally efficient solver to facilitate scattering simulations of realistic forest scenes for airborne foliage-penetration radar applications.

15. SUBJECT TERMS
analytical solution, discrete scatterer technique, electromagnetic scattering, foliage-penetration radar, tree scattering

16. SECURITY CLASSIFICATION OF:			17. LIMITATION OF ABSTRACT	18. NUMBER OF PAGES	19a. NAME OF RESPONSIBLE PERSON
a. REPORT	b. ABSTRACT	c. THIS PAGE	UU	30	DaHan Liao
Unclassified	Unclassified	Unclassified			19b. TELEPHONE NUMBER (Include area code) (301) 394-1741

Contents

List of Figures

1. Introduction

Developing sensing capabilities for the detection of ground targets concealed in a forest environment necessitates a fundamental understanding of the scattering properties of not only the targets and the trees but also their interactions over the observation time interval. For a given target in motion under the tree canopy, the time-frequency behaviors of these scattering interactions are very much dependent upon the tree arrangement and the precise structure of the canopy. In this respect, the spatial distribution of the various tree constituents (trunks, branches, and foliage) potentially becomes an important determinant of the detection performance of the radar sensor and processing algorithm, and therefore, needs to be preserved in a wave scattering solver. For example, in the application of a clutter-limited technique such as along-track interferometry for moving target indication, the trees surrounding the target can introduce deleterious effects into the interferometric phase, leading to decorrelation and a nonlinear target phase-velocity relationship, as a result of tree occlusion, attenuation, and phase distortion. From the radar simulation perspective, such effects can only be studied with a physics-based solver that faithfully captures the actual positions of the target and the trees and their scattering phase centers over the entire coherent processing interval.

Existing foliage-penetration radar performance analysis tools are rather simplistic in that they do not take into account the localized interactions of the target with its surrounding, nor do they fully consider the polarimetric scattering responses of the scene (i.e., the target and clutter responses are often rudimentarily incorporated into the signal model just by using radar cross section values or coefficients). Higher fidelity scattering analysis in the form of the discrete scatterer technique (DST) has been undertaken in the microwave remote sensing community within the context of developing algorithms for retrieving tree/forest biophysical parameters from the scattering returns.[1,2] In Lin and Sarabandi,[1] wave theory is applied in constructing a 3-D coherent scattering model for forest stands consisting of fractal-generated trees; unfortunately, in this model, although individual trees have deterministic positions, the propagation or transmissivity effects of the trees are considered only in a statistical manner within a layered-canopy representation. A similar approach to that of Lin and Sarabandi[1] is also employed by Thirion et al.,[2] wherein the main physical features of the canopy such as the trunks and crown shapes are captured, but the branches and leaves are specified only indirectly through probability distributions.

Moreover, notwithstanding the usefulness of the analytical solvers developed in these aforementioned studies, and others not discussed here,[3–6] the application

focus in existing works has not been on the detection of moving targets under the canopy but rather only on the responses of the trees themselves. It should be noted that a variety of radiative transfer-based solvers also have been put forth for tree response characterization. While traditional radiative transfer theory has been applied successfully to a number of remote sensing scenarios—some involving complex forest canopy structures[7]—this method does not include the coherent scattering effects occurring within the tree structure and therefore cannot be used to compute the phase response of a scene.

In order to account for the spatial distribution of the trees coherently and systematically, this work follows the framework proposed by Liu et al.,[8] in which a multi-ray approach is exploited to calculate the aggregate scattered fields from a collection of trees, with the transmissivity of each ray determined from a cell-based representation of the scene. A cell-by-cell, interaction-tracking procedure is also proposed here for speeding up the calculations of the responses from small components such stems and leaves, which are expected to far outnumber those scatterers composing the main trunks. Furthermore, tree and scene generation for the analytical solver is carried out in conjunction with that for a large-scale, full-wave solver, allowing for an assessment of the accuracy of the ray-based solution for any scene. Note that the details of the full-wave solver itself have been published elsewhere,[9] which demonstrated the practicality of finite-difference time-domain (FDTD)-based scattering simulations of a realistic forest scene for foliage-penetration radar applications.

In brief, this work is organized as follows. In Section 2, an overview of the procedure for generating 3-D realistic trees for both the analytical and numerical solvers is presented. In Section 3, the formulations for the DST are described in detail. In Section 4, computational examples are given: the DST solutions are compared with full-wave simulation results; the accuracy of the cell-by-cell approach is evaluated; and a general discussion on the scattering effects of a forest stand is put forth. Finally, Section 5 summarizes the study.

2. Tree Generation

Realistic 3-D tree structures are created using the open-source tree generation engine Arbaro,[10] which implements the recursive, rule-based, growth algorithm developed by Weber and Penn.[11] Given a random seed and an input parameter file defining the physical characteristics of a tree (e.g., tree and trunk shape, number of branch levels, branch sizes and angles, leaf shape and density), the algorithm constructs the hierarchical structure for the tree by following a series of recursive rules derived from geometrical observables. For the DST solver of this work, each

tree is exported from Arbaro as a multilevel Persistence of Vision Raytracer (POV-ray) file in which the trunk/branches and leaves are represented by tube and disk primitives, respectively. Additional geometric transformation or processing of the exported tree object (i.e., decomposition of the tube primitives into cylinders of desired sizes, global translation, and scaling, etc.) is carried out before the entire model is passed on to the scattering solver. For the FDTD-based simulations, the mesh form of the tree structure is first exported from Arbaro as a Wavefront OBJ file; subsequently, voxelization of the mesh is performed using the parity count and ray stabbing methods.[9,12–13]

3. Cell-Based Discrete Scatterer Technique

Once the trees have been parsed into canonical components or scatterers (i.e., dielectric cylinders and disks), each with deterministic locations and well-defined physical and electrical properties, the scattering solver is derived by applying the 3-step procedure as follows. First, the tree scene—consisting N_t trees—is discretized into N_b cubic cells (Fig. 1), with each scatterer assigned to a cell. Second, the propagation paths for each scatterer are identified and tabulated: this necessitates deducing all the cells intercepted by the 4 rays shown in Fig. 2. Finally, the ray-based scattering response for each scatterer is calculated analytically, while taking into consideration the effects of attenuation and phase change encountered along each ray path, and then the total scattering response of the entire scene is obtained by coherently summing the returns from all the scatterers. Succinctly, in the multi-ray approach, for incident direction $\hat{k}_i$ and scattering direction $\hat{k}_s$, the scattering matrix for the nth ($n \in \{1,2,...,N_c\}$) scatterer can be written as

$$\overline{\overline{S}}^n\left(\hat{k}_s,\hat{k}_i\right)=\overline{\overline{S}}_c^n\left(\hat{k}_s,\hat{k}_i\right)+\overline{\overline{S}}_{cg}^n\left(\hat{k}_s,\hat{k}_i\right)+\overline{\overline{S}}_{gc}^n\left(\hat{k}_s,\hat{k}_i\right)+\overline{\overline{S}}_{gcg}^n\left(\hat{k}_s,\hat{k}_i\right), \quad (1)$$

where

$$\overline{\overline{S}}_c^n\left(\hat{k}_s,\hat{k}_i\right)=\overline{\overline{T}}_c^n\left(\hat{k}_s\right)\cdot\overline{\overline{S}}^{fs,n}\left(\hat{k}_s,\hat{k}_i\right)e^{-jk_o\left(\hat{k}_i\cdot\vec{r}_o^{\,n}-\hat{k}_s\cdot\vec{r}_o^{\,n}\right)}\cdot\overline{\overline{T}}_c^n\left(\hat{k}_i\right); \quad (2)$$

$$\overline{\overline{S}}_{cg}^n\left(\hat{k}_s,\hat{k}_i\right)=\overline{\overline{T}}_c^n\left(\hat{k}_s\right)\cdot\overline{\overline{S}}^{fs,n}\left(\hat{k}_s,\hat{k}_{gi}\right)e^{-jk_o\left(\hat{k}_i\cdot\vec{r}_g^{\,n}-\hat{k}_s\cdot\vec{r}_o^{\,n}\right)}\cdot\overline{\overline{T}}_{cg}^n\left(\hat{k}_{gi}\right)\cdot\overline{\overline{\Gamma}}\left(\hat{k}_i\right)\cdot\overline{\overline{T}}_g^n\left(\hat{k}_i\right); \quad (3)$$

$$\overline{\overline{S}}_{gc}^n\left(\hat{k}_s,\hat{k}_i\right)=\overline{\overline{T}}_g^n\left(\hat{k}_s\right)\cdot\overline{\overline{\Gamma}}\left(\hat{k}_s\right)\cdot\overline{\overline{T}}_{gc}^n\left(\hat{k}_{gs}\right)\cdot\overline{\overline{S}}^{fs,n}\left(\hat{k}_{gs},\hat{k}_i\right)e^{-jk_o\left(\hat{k}_i\cdot\vec{r}_o^{\,n}-\hat{k}_s\cdot\vec{r}_g^{\,n}\right)}\cdot\overline{\overline{T}}_c^n\left(\hat{k}_i\right); \quad (4)$$

$$\overline{\overline{S}}^{n}_{gcg}\left(\hat{k}_s,\hat{k}_i\right)=\overline{\overline{T}}^{n}_{g}\left(\hat{k}_s\right)\cdot\overline{\overline{\Gamma}}\left(\hat{k}_s\right)\cdot\overline{\overline{T}}^{n}_{gc}\left(\hat{k}_{gs}\right)\cdot\overline{\overline{S}}^{fs,n}\left(\hat{k}_{gs},\hat{k}_{gi}\right)e^{-jk_o\left(\hat{k}_i\cdot\vec{r}_g^{\,n}-\hat{k}_s\cdot\vec{r}_g^{\,n}\right)}\cdot\overline{\overline{T}}^{n}_{cg}\left(\hat{k}_{gi}\right)\cdot\overline{\overline{\Gamma}}\left(\hat{k}_i\right)\cdot\overline{\overline{T}}^{n}_{g}\left(\hat{k}_i\right);\quad(5)$$

in which $\vec{r}_o^{\,n}$ is the location of the scatterer center; $\vec{r}_g^{\,n}=\vec{r}_o^{\,n}-2\left(\vec{r}_o^{\,n}\cdot\hat{z}\right)\hat{z}$; $\hat{k}_{gi}=\hat{k}_i-2\left(\hat{k}_i\cdot\hat{z}\right)\hat{z}$; $\hat{k}_{gs}=\hat{k}_s-2\left(\hat{k}_s\cdot\hat{z}\right)\hat{z}$; $\overline{\overline{S}}^{fs,n}(\cdot,\cdot)$ is the scatterer free-space response; $\overline{\overline{T}}^{n}_{u}(\cdot)$ (u = c, g, cg, gc) is the transmissivity matrix of the propagation path as determined by the cells intercepted; and $\overline{\overline{\Gamma}}(\cdot)$ is the ground reflection coefficient matrix. Essentially, in the presence of the ground, the multi-ray technique captures the first 4 orders of scattering effects: Eq. 2 is the direct scattering response from the scatterer; Eqs. 3 and 4 correspond to the single ground-bounce returns; and Eq. 5 is the double ground-bounce contribution.

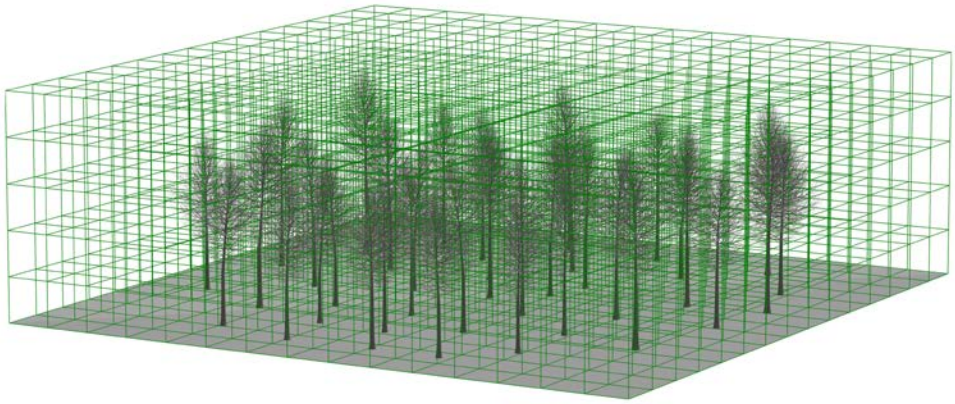

Fig. 1 Cellularized DST computational domain

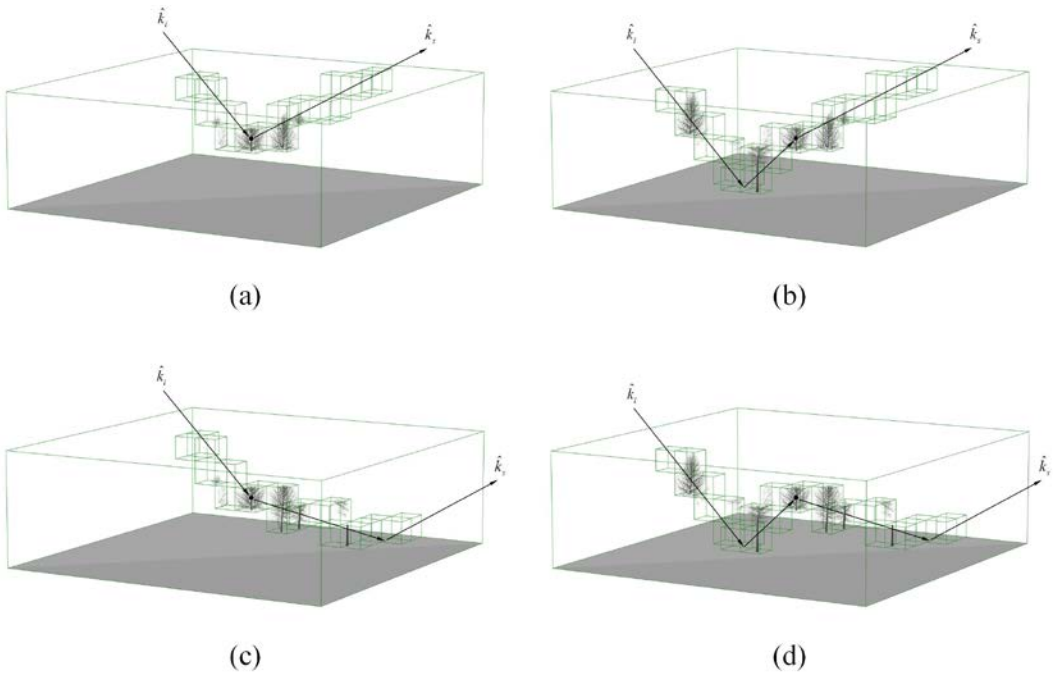

Fig. 2 Ray paths for a scatterer: a) direct response, b-c) single ground-bounce returns, and d) double ground-bounce return

In Eqs. 2–5, the free-space response of the scatterer, $\overline{\overline{S}}^{fs,n}(\cdot,\cdot)$, is derived with the application of 2 sets of approximate formulations: for a finite-length, circular cylinder scatterer, the volumetric current integration method is employed wherein the internal cylinder fields are assumed to be the same as those of the infinite-length case;[14,15] and for a thin-disk scatterer, the generalized Rayleigh-Gans solution is applied wherein the internal disk fields are related to the incident fields through the polarizability tensor of the scatterer.[15] In the current work, the leaves are simply modeled as circular disks. The analytical formulations for these 2 sets of solutions are included in the Appendix.

The aforementioned transmissivity matrix

$$\overline{\overline{T}}_u^n(\cdot)=\begin{bmatrix} T_{u,vv}^n(\cdot) & T_{u,vh}^n(\cdot) \\ T_{u,hv}^n(\cdot) & T_{u,hh}^n(\cdot) \end{bmatrix} \tag{6}$$

is calculated with Foldy's approximation,[16] which derives the distortion effects of a random medium on a mean field. It can be shown that

$$T_{u,pp}^n(\cdot)=e^{-j\vec{\mathrm{K}}_{pp}(\cdot)\cdot\vec{\ell}_u^n(\cdot)},\ pp=vv,hh; \tag{7}$$

and, assuming a medium with azimuthal symmetry, $T_{u,hv}^n(\cdot)=T_{u,vh}^n(\cdot)=0$. In Eq. 7, $\vec{\ell}_u^n(\cdot)\in \mathrm{R}^{N_b}$ is the propagation path length vector (i.e., the bth element of $\vec{\ell}_u^n(\cdot)$ is

the path length of the ray in cell b, $b \in \{1,2,...,N_b\}$); and $\vec{K}_{pp}(\cdot) \in \mathbb{C}^{N_b}$ is the aggregate forward scattering vector for all the cells, with its bth element computed as

$$\kappa_{pp}^{b}(\cdot) = \frac{2\pi}{k_o v} \sum_{m \in \text{cell } b} S_{pp}^{fs,m}(\cdot,\cdot), \tag{8}$$

where v is the cell volume. Together, Eqs. 1–8 give the most general framework for analyzing the scattering from a tree scene, taking into account propagation attenuation and phase change effects experienced by the incident and scattered waves for each discrete scatterer in the random medium. In view of the fact that the scatterers that compose the tree trunks are the largest scatterers in the scene and therefore would provide the dominant responses, extra consideration must be taken in evaluating Eq. 6 for the trunk elements. In most realistic scenarios, the individual scatterers of a trunk are not expected to be shadowed by other scatterers belonging to the same trunk—in other words, a trunk cannot shadow itself. As such, in calculating the transmissivity matrices for the scatterers of a particular tree trunk t ($n \in \text{trunk } t, t \in \{1,2,...,N_t\}$), the effects of self-shadowing should be excluded by modifying Eq. 8 as

$$\kappa_{pp}^{b}(\cdot) = \sum_{\substack{m \in \text{cell } b \\ m \notin \text{trunk } t}} S_{pp}^{fs,m}(\cdot,\cdot). \tag{9}$$

To increase the computational efficiency of the solver, instead of a scatterer-by-scatterer brute force approach, a cell-by-cell scattering and propagation strategy can be applied for the treatment of the smallest branch elements and the leaves, which are expected to far outnumber those scatterers composing the trunks and larger branches. In this approach, all the constituents of a cell are assumed to have the same set of transmissivity matrices (for each ray path) and the responses are propagated together as a group rather than one by one. To this end, the approximation is made such that the ray paths of all the scatterers belonging to the same cell are identical. Here, the center of the cell is used as the common reference point for identifying all those paths and evaluating the transmissivity matrices using Eqs. 6–8. The accuracy of the previous approximation is investigated in the next section.

Essentially, in this cell-by-cell strategy, computational speedup is provided by not having to calculate the transmissivity matrices on a scatterer-by-scatterer basis, as well as by not having to determine and tabulate the ray paths for every scatterer in a cell. Note that the same cell-based strategy can potentially be applied to the scatterers for the trunks and larger branches, as well. However, in general, since

those scatterers are expected to provide the more dominant responses—as compared to the smallest branches and the leaves, the associated errors induced by the underlying assumptions of the technique are also expected to be more significant.

4. Numerical Results

The scenes of interest are displayed in Fig. 3, which shows a forest stand composed of $N_t = 72$ randomly generated quaking aspen (*Populus tremuloides*) trees modeled with different levels of structural fidelity. The trees are constructed assuming a 4-level hierarchy—as such, there are 4 cases of consideration: the trunks only, the trunks with primary branches, the trunks with primary and secondary branches, and the trees with all their branches and leaves. As the starting point, the backscattering returns of the forest stand are first examined by comparing the DST results with those from the full-wave solver. Note that since the FDTD method as employed here cannot efficiently model extremely thin structures such as leaves, validation of the DST results is only carried out for scene configurations without the foliage.

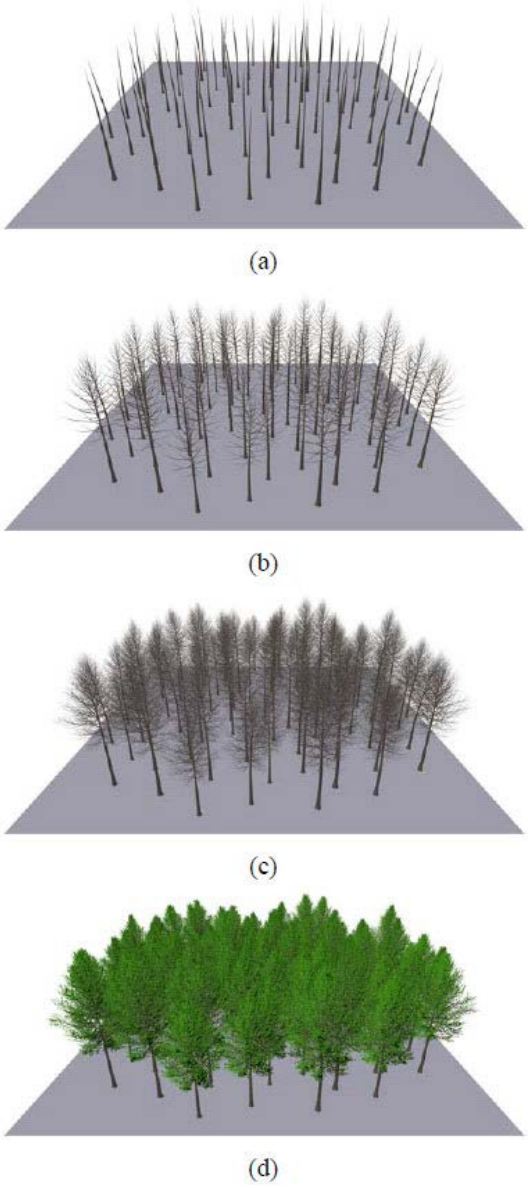

Fig. 3 Forest stand with 72 randomly generated trees: a) tree trunks only, N_c = 2017, b) tree trunks + primary branches, N_c = 25397, c) tree trunks + primary and secondary branches, N_c = 292877, and d) tree trunks + primary and secondary branches + leaves, N_c = 1878880

The FDTD- and DST-calculated backscattering radar cross sections σ_{pq} ($p,q = v,h$) and phase differences ξ_d ($d = c,x$) of the forest stand are illustrated in Figs. 4–6, as a function of the elevation incidence angle θ_i and structural fidelity. Formally, the plotted co- and cross-polarized responses are defined as follows: $\sigma_{pq} = 4\pi\left|\left\langle S_{pq}\right\rangle\right|^2$, $\xi_c = \arg\left\langle S_{vv}S_{hh}^*\right\rangle$, and $\xi_x = \arg\left\langle S_{vv}S_{hv}^*\right\rangle$, where S_{pq} is the pq-polarized scattering matrix element. Note that in the backscattering direction,

$S_{hv} = -S_{vh}$. The results at each elevation incidence angle are obtained by averaging the responses over 36 evenly spaced azimuth incidence angles spanning ϕ_i = [0°, 360°] and over 301 frequencies spanning f = [200 MHz, 500 MHz] (P-band). The ground and the tree trunk/branches are assumed to be electrically homogeneous, with relative dielectric constant and conductivity (ε_r, σ_d) of (5.45, 20 mS/m) and (13.9, 39 mS/m), respectively. The FDTD computational domain has dimensions 30 m × 30 m × 9.2 m and is discretized into 2 billion voxels; parallelized simulations are performed after partitioning each scene into 256 subdomains.[9] On the other hand, the DST scene has dimensions 30 m × 30 m × 10 m and is divided into N_b = 9,000 cubic cells (i.e., each cell has a side length of 1 m).

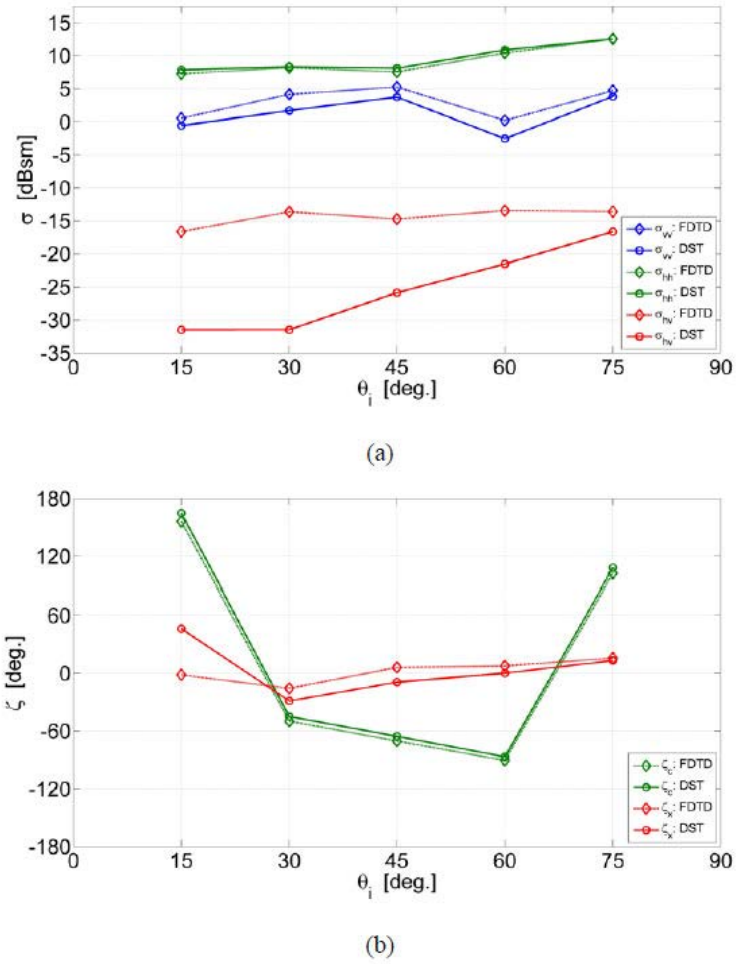

Fig. 4 Comparison of DST solution with FDTD solution for scene containing trunks only (Fig. 3a): a) radar cross sections and b) phase differences

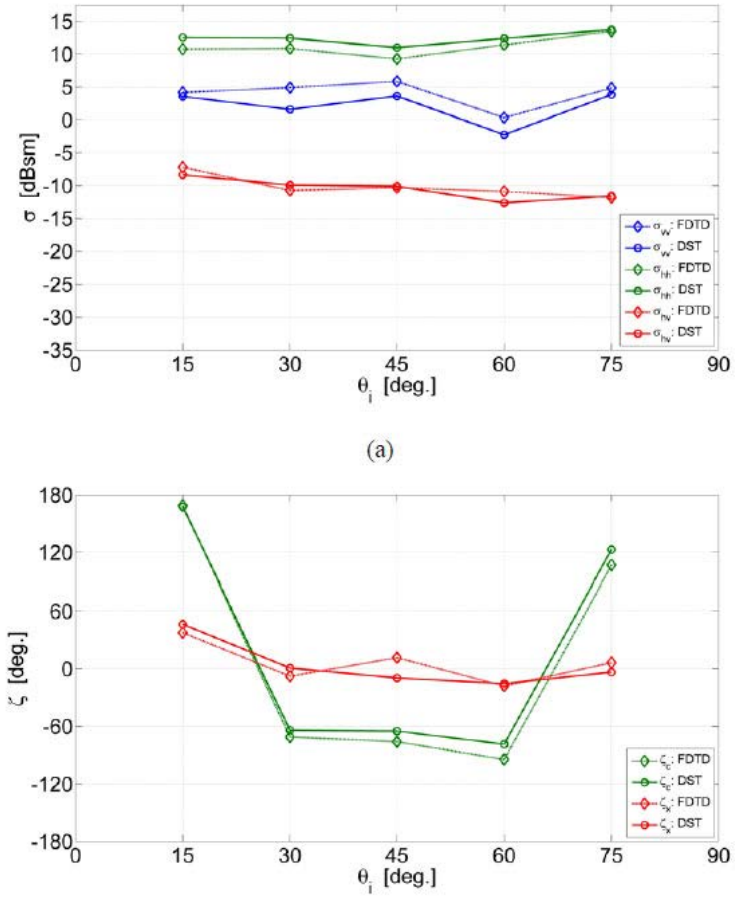

Fig. 5 Comparison of DST solution with FDTD solution for scene containing trunks + primary branches (Fig. 3b): a) radar cross sections and b) phase differences

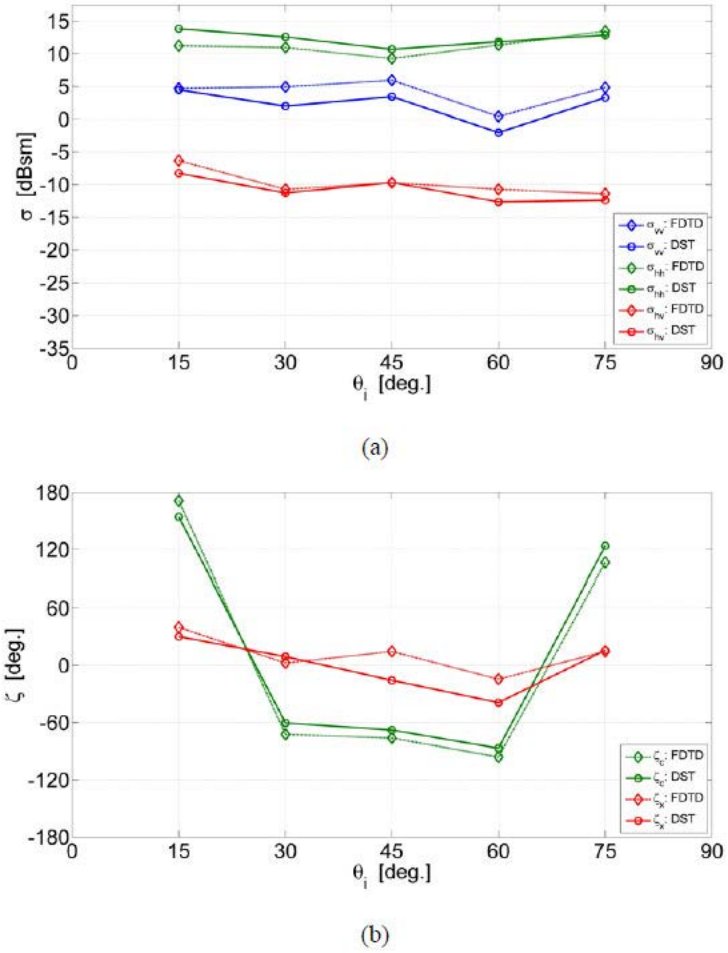

Fig. 6 Comparison of DST solution with FDTD solution for scene containing trunks + primary and secondary branches (Fig. 3c): a) radar cross sections and b) phase differences

As evident from Figs. 4–6, in general, except for the cross-polarized response of the trunks-only scene (Fig. 4), the DST results are in good agreement with those from the full-wave method—in both amplitude and phase. For the trunks-only scene, the observed discrepancy between the analytical and numerical cross-polarized returns is in part due to the fact that the FDTD solver as implemented here cannot capture low cross-polarization signal levels. Once the branches are introduced into the scene, the cross-polarized response increases; therefore, those cases with the branches (Figs. 5 and 6) do not pose a problem for the FDTD solver. Note that at the cost of increased computational time and memory, the fidelity of the numerical cross-polarized solution can be improved by reducing the FDTD voxel size. Although the limitation of the full-wave analysis here precludes a complete validation of the DST results when the cross-polarized response is low, the DST co-polarized solutions are seen to match those from FDTD reasonably well in all cases.

The analytical solutions presented thus far are obtained by calculating the responses from the scene on a scatterer-by-scatterer basis. To speed up the computations, the cell-by-cell interaction algorithm discussed in Section 3 is applied for the treatment of the secondary branches in the scene in Fig. 3c. A comparison of the results from this new approach with those from the original scatterer-by-scatterer technique is shown in Fig. 7. It is observed that the more computationally efficient approach retains the accuracy of the brute force technique. Note that the memory usage and runtime for the scatterer-by-scatterer simulation are 369 MB and 33 min/frequency, respectively, on a Dell Precision T7500 workstation with Intel Xeon CPU of 2.67 GHz, while those for the cell-by-cell simulation are 200 MB and 40 s/frequency, respectively.

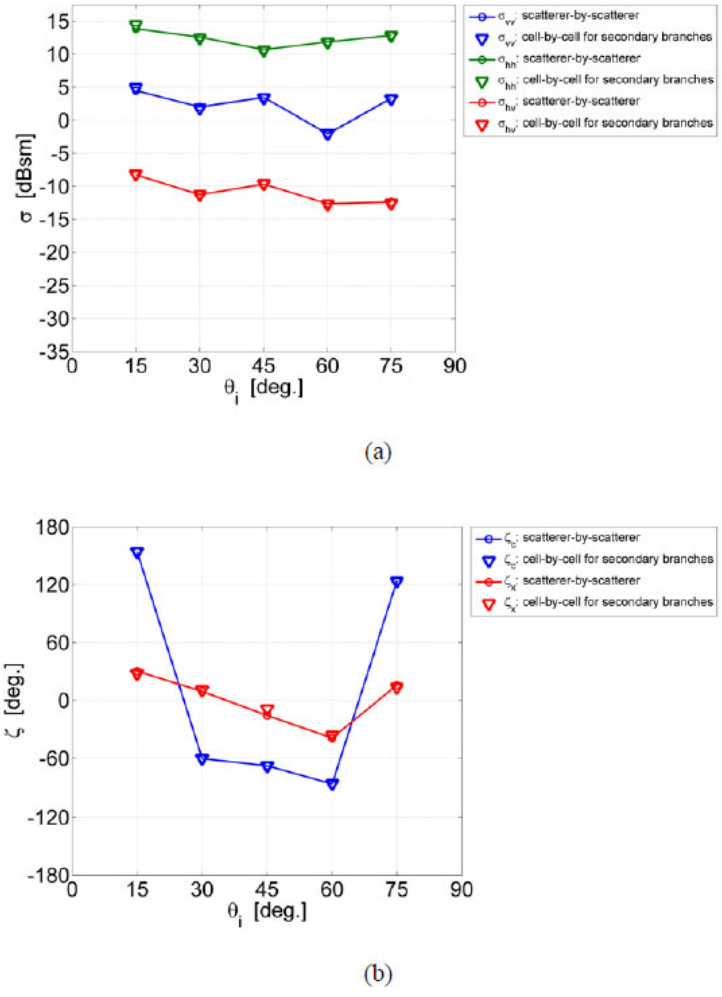

Fig. 7 Comparison of scatterer-by-scatterer vs. cell-by-cell DST solutions for scene containing trunks + primary and secondary branches (Fig. 3c): a) radar cross sections and b) phase differences

The DST-simulated backscattering responses of the forest stand for the 4 levels of scene structural fidelity are plotted together in Figs. 8 and 9. The foliage is modeled by considering the leaves as circular dielectric disks with a thickness of 0.2 mm, a mean radius of 2.6 cm, and (ε_r, σ_d) = (28.0, 0.37 S/m). The cell-by-cell strategy is implemented for the secondary branches and the leaves when the scene contains those components. (The memory usage and runtime for the case with all the branches and leaves are 1.0 GB and 56 s/frequency, respectively.) For the co-polarized responses, it is noted that as the elevation incidence angle increases, the dominant contribution tends to be provided by the tree trunks—though this is more apparent for *hh* than *vv*. In general, the inclusion of the primary branches is seen to lead to an enhanced backscattering intensity, compared to the response of the scene with only the trunks. However, further addition of the secondary branches and the leaves to the scene can weaken the return—especially at the higher incidence angles where the propagation loss of the canopy plays a more important role. Unlike the co-polarized returns, the cross-polarized response of the forest stand is mainly determined by the primary branches and not by the trunks. This is as expected, since the trunks here resemble slightly asymmetric cones that have only a small cross-polarized backscattering response. As in the co-polarized cases, the inclusion of the secondary branches and the leaves tends to decrease the cross-polarized return, relative to that for the scene with only the trunks and the primary branches.

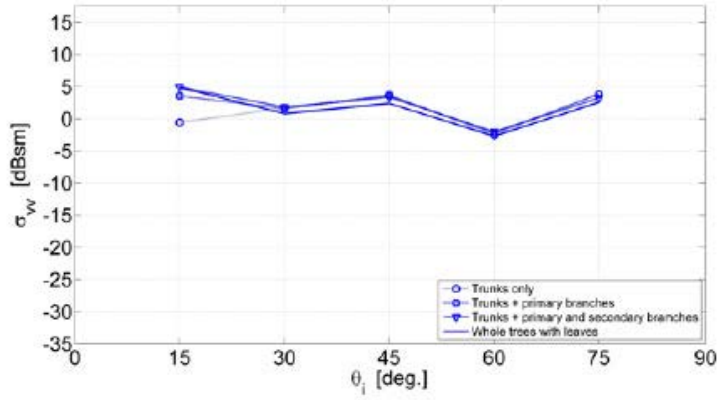

(a)

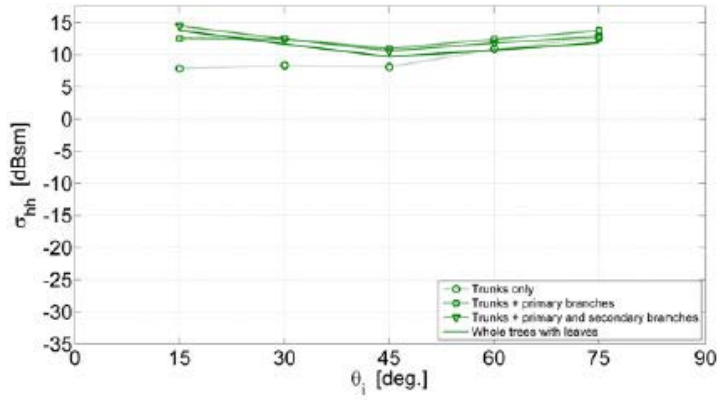

(b)

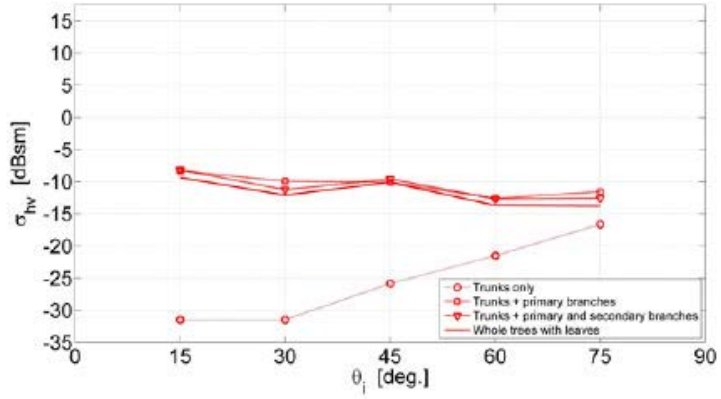

(c)

Fig. 8 Radar cross sections of the scenes in Fig. 3: a) σ_{vv}, b) σ_{hh}, and c) σ_{hv}

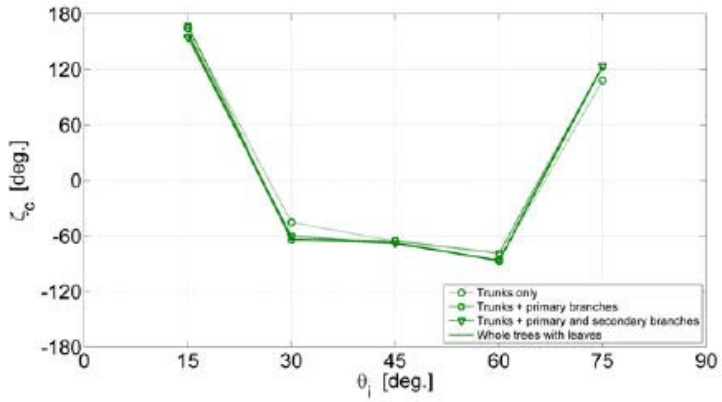

(a)

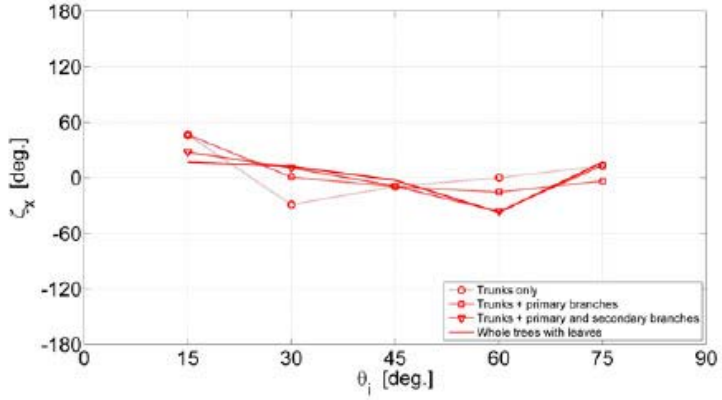

(b)

Fig. 9 Phase differences of the scenes in Fig. 3: a) ξ_c and b) ξ_x.

5. Conclusions

An analytical solver is developed in this study for characterizing the far-field electromagnetic scattering responses of trees. The solution is based on a multi-ray discrete scatterer approach, applicable to a cellularized scene comprising realistic 3-D tree structures of which the constituents are represented by cylinders and disks. The accuracy of the solver is determined by comparing the backscattering results for a forest stand at P-band with those from large-scale, full-wave simulations. A cell-by-cell strategy is also proposed and implemented to increase the computational efficiency of the solver for evaluating the scattering contributions from the smallest branches and the leaves. Overall, the analysis and computational framework put forth is intended as a tool for investigating scattering effects relevant to airborne foliage-penetration radar applications.

6. References

1. Lin Y-C, Sarabandi K. A Monte Carlo coherent scattering model for forest canopies using fractal-generated trees. IEEE Trans Geoscience and Remote Sensing. 1999 Jan;37(1):440–451.

2. Thirion L, Colin E, Dahon C. Capabilities of a forest coherent scattering model applied to radiometry, interferometry, and polarimetry at P- and L-band. IEEE Trans Geoscience and Remote Sensing. 2006 Apr;44(4):849–862.

3. Zeng T, Hu C, Sun H, Chen E. A novel rapid SAR simulator based on equivalent scatterers for three-dimensional forest canopies. IEEE Trans Geoscience and Remote Sensing. 2014 Sep;52(9):5243–5255.

4. Jiang W-Q, Zhang M, Chen H, Lu Y-G. CUDA implementation in the EM scattering of a three-layer canopy. Prog Electromagn Res. 2011;116:457–473.

5. Williams ML, Pottier E, Ferro-Famil L, Allain S, Cloude SR, Hajnsek I, Papathanassiou K, Moreira A. Forest coherent SAR simulation within PolSARpro: an educational toolbox for PolSAR and PolInSAR data processing. ACRS 2007. Proceedings of the Asian Conference on Remote Sensing; 2007 Nov 12–17; Kuala Lumpur, Malaysia.

6. Chauhan NS, Lang RH, Ranson KJ. Radar modeling of a boreal forest. IEEE Trans Geoscience and Remote Sensing. 1991 Jul;29(4):627–638.

7. Liang P, Moghaddam M, Pierce LE, Lucas RM. Radar backscattering model for multilayer mixed-species forests. IEEE Trans Geoscience and Remote Sensing. 2005 Nov;43(11):2612–2626.

8. Liu D, Sun G, Guo Z, Ranson KJ, Du Y. Three-dimensional coherent radar backscatter model and simulations of scattering phase center of forest canopies. IEEE Trans Geoscience and Remote Sensing. 2010 Jan;48(1):349–357.

9. Liao DH, Dogaru T. Full-wave scattering and imaging characterization of realistic trees for FOPEN sensing. IEEE Geoscience Remote Sensing Lett. 2016 Jul;13(7):957–961.

10. Diestel W. Arbaro—Tree generation for POV-Ray; n.d. [accessed 2016]. http://arbaro.sourceforge.net.

11. Weber J, Penn J. Creation and rendering of realistic trees. SIGGRAPH 1995. Proceedings of the 22nd Annual Conference on Computer Graphics and Interactive Techniques; 1995 Aug 6–11; Los Angeles, CA.

12. Min P. Binvox—3D mesh voxelizer; 2016 Mar [accessed 2016]. http://cs.princeton.edu/~min/binvox.

13. Nooruddin FS, Turk G. Simplification and repair of polygonal models using volumetric techniques. IEEE Trans Vis and Comput Graph. 2003;9:191–205.

14. Liao DH. Scattering from the finite-length, dielectric circular cylinder: Part I—derivation of an analytical solution. Adelphi (MD): Army Research Laboratory (US); 2015. Report No.: ARL-TR-7346.

15. Karam MA, Fung AK, Antar YMM. Electromagnetic wave scattering from some vegetation samples. IEEE Trans Geoscience and Remote Sensing. 1988 Nov;26(6):799–808.

16. Tsang L, Kong JA, Shin R. Theory of microwave remote sensing. New York (NY): Wiley-Interscience; 1985.

INTENTIONALLY LEFT BLANK.

Appendix. Scattering Solution for Branch and Leaf Scatterers

Analytical formulations for calculating the electromagnetic scattering responses of tree branches and leaves are given. Note that the following treatment assumes the incident and scattered wave directions ($\hat{k}_i$, $\hat{k}_s$) and their associated polarization vectors ($\hat{h}$, $\hat{v}$) are defined by

$$\hat{k}_i = \sin\theta_i \cos\phi_i \hat{x} + \sin\theta_i \sin\phi_i \hat{y} - \cos\theta_i \hat{z}; \tag{A-1}$$

$$\hat{k}_s = \sin\theta_s \cos\phi_s \hat{x} + \sin\theta_s \sin\phi_s \hat{y} + \cos\theta_s \hat{z}; \tag{A-2}$$

$$\hat{h}_{i,s} = \frac{\hat{z} \times \hat{k}_{i,s}}{\left| \hat{z} \times \hat{k}_{i,s} \right|}; \tag{A-3}$$

$$\hat{v}_{i,s} = \hat{h}_{i,s} \times \hat{k}_{i,s}; \tag{A-4}$$

in which the subscripts *i* and *s* identify quantities related to the incident and scattered waves, respectively; θ_i is the incidence angle in elevation (measured from $-\hat{z}$); θ_s is the scattering angle in elevation (measured from $+\hat{z}$); and $\phi_{i,s}$ is the incidence/scattering angle in azimuth (measured from $+\hat{x}$).

A-1 Scattering from Branches

In this study, the tree branches are approximated with circular cylinders. The free-space scattering matrix elements of a finite-length, dielectric circular cylinder with length *L*, radius *a*, and complex relative dielectric constant $\varepsilon_{r,t}$ are derived as[1,2]

$$S_{pq}^{fs}\left(\hat{k}_s, \hat{k}_i\right) = \hat{p}_s \cdot \frac{k_o^2 \left(\varepsilon_{r,t} - 1\right) L}{2} \operatorname{sinc}\left(\frac{k_o L \left(\cos\theta_i + \cos\theta_s\right)}{2} \right) \sum_{n=-\infty}^{+\infty} \left[\vec{\mathrm{K}}_{1,n} + \vec{K}_{2,n} + \vec{K}_{3,n} \right] e^{jn(\phi_s - \phi_i)}, \; p, q = v, h \tag{A-5}$$

where

$$\vec{\mathrm{K}}_{1,n} = \frac{j k_o I_{n+1} e^{j\phi_s}}{2 k_{\rho,r}} \left(\beta_n - j\alpha_n\right)\left(\hat{x} - j\hat{y}\right); \quad \vec{\mathrm{K}}_{2,n} = -\frac{j k_o I_{n-1} e^{-j\phi_s}}{2 k_{\rho,r}} \left(\beta_n + j\alpha_n\right)\left(\hat{x} + j\hat{y}\right); \; \vec{\mathrm{K}}_{3,n} = I_n \gamma_n \hat{z}. \tag{A-6}$$

For $q = v$,

$$\alpha_n = \frac{j M_n \sin\theta_i \cos\theta_i}{J_n\left(k_{\rho,r} a\right) R_n}; \;\; \beta_n = \frac{nW \sin\theta_i \cos\theta_i}{J_n\left(k_{\rho,r} a\right) R_n}; \; \gamma_n = \frac{j M_n \sin\theta_i}{J_n\left(k_{\rho,r} a\right) R_n}; \tag{A-7}$$

[1] Liao DH. Scattering from the finite-length, dielectric circular cylinder: Part I—derivation of an analytical solution. Adelphi (MD): Army Research Laboratory (US); 2015. Report No.: ARL-TR-7346.

[2] Karam MA, Fung AK, Antar YMM. Electromagnetic wave scattering from some vegetation samples. IEEE Trans Geoscience and Remote Sensing. 1988 Nov;26(6):799–808.

for $q = h$,

$$\alpha_n = \frac{nW \sin\theta_i \cos^2\theta_i}{J_n\left(k_{\rho,r}a\right)R_n};\ \ \beta_n = \frac{-jN_n \sin\theta_i}{J_n\left(k_{\rho,r}a\right)R_n};\ \gamma_n = \frac{nW \sin\theta_i \cos\theta_i}{J_n\left(k_{\rho,r}a\right)R_n}; \tag{A-8}$$

and

$$I_n = \frac{a^2}{\left(k_{\rho,r}a\right)^2 - \left(k_{\rho,s}a\right)^2}\left(k_{\rho,r}aJ_n\left(k_{\rho,s}a\right)J_{n+1}\left(k_{\rho,r}a\right) - k_{\rho,s}aJ_n\left(k_{\rho,r}a\right)J_{n+1}\left(k_{\rho,s}a\right)\right); \tag{A-9}$$

$$R_n = \frac{\pi\left(k_{\rho,i}a\right)^2 H_n^{(2)}\left(k_{\rho,i}a\right)}{2}\cdot\left[M_n \cdot N_n - W^2 n^2 \cos^2\theta_i\right]; \tag{A-10}$$

$$M_n = \frac{H_n^{(2)\prime}\left(k_{\rho,i}a\right)}{k_{\rho,i}aH_n^{(2)}\left(k_{\rho,i}a\right)} - \frac{J_n'\left(k_{\rho,r}a\right)}{k_{\rho,r}aJ_n\left(k_{\rho,r}a\right)}; \tag{A-11}$$

$$N_n = \frac{H_n^{(2)\prime}\left(k_{\rho,i}a\right)}{k_{\rho,i}aH_n^{(2)}\left(k_{\rho,i}a\right)} - \varepsilon_{r,t}\frac{J_n'\left(k_{\rho,r}a\right)}{k_{\rho,r}aJ_n\left(k_{\rho,r}a\right)}; \tag{A-12}$$

$$W = \frac{1}{\left(k_{\rho,i}a\right)^2} - \frac{1}{\left(k_{\rho,r}a\right)^2}. \tag{A-13}$$

The previous equations assume $k_{\rho,i} = k_o \sin\theta_i$, $k_{\rho,s} = k_o \sin\theta_s$, and $k_{\rho,r} = k_o\sqrt{\varepsilon_{r,t} - \cos^2\theta_i}$.

A-2 Scattering from Leaves

The scattering response of a circular disk-shaped leaf with thickness τ, radius a, and complex relative dielectric constant $\varepsilon_{r,t}$ is given by

$$S_{pq}^{fs}\left(\hat{k}_s, \hat{k}_i\right) = \frac{k_o^2 v_c}{\pi}\cdot\frac{J_1\left(Q_{si}a\right)}{Q_{si}a}\left(\varepsilon_{r,t} - 1\right)\left[a_T\left(\hat{p}_s \cdot \hat{q}_i\right) + \left(a_N - a_T\right)\left(\hat{p}_s \cdot \hat{z}\right)\left(\hat{z} \cdot \hat{q}_i\right)\right],\ \ p, q = v, h \tag{A-14}$$

where

$$v_c = \frac{a^2\tau\pi}{2}; \tag{A-15}$$

$$a_T = \frac{1}{\left(\varepsilon_{r,t} - 1\right)g_T + 1}; \tag{A-16}$$

$$a_N = \frac{1}{\left(\varepsilon_{r,t} - 1\right) g_N + 1}; \tag{A-17}$$

$$g_T = \frac{1}{2\left(m^2 - 1\right)} \cdot \left[\frac{m^2}{\sqrt{m^2 - 1}} \sin^{-1}\left(\frac{\sqrt{m^2 - 1}}{m} \right) - 1 \right]; \tag{A-18}$$

$$g_N = \frac{m^2}{m^2 - 1} \cdot \left[1 - \frac{1}{\sqrt{m^2 - 1}} \sin^{-1}\left(\frac{\sqrt{m^2 - 1}}{m} \right) \right]; \tag{A-19}$$

$$m = \frac{2a}{\tau}; \tag{A-20}$$

$$Q_{si} = k_o \left(\sin^2 \theta_s + \sin^2 \theta_i - 2 \sin \theta_s \sin \theta_i \cos\left(\phi_s - \phi_i\right) \right)^{\frac{1}{2}}. \tag{A-21}$$

1 (PDF) DEFENSE TECHNICAL INFORMATION CTR DTIC OCA

2 (PDF) DIRECTOR US ARMY RESEARCH LAB RDRL CIO L IMAL HRA MAIL & RECORDS MGMT

1 (PDF) GOVT PRINTG OFC A MALHOTRA

3 (PDF) DIRECTOR US ARMY RESEARCH LAB RDRL SER U TRAIAN DOGARU DAHAN LIAO ANDERS SULLIVAN

INTENTIONALLY LEFT BLANK.